Effect of ultra-fast pyrolysis on polymer-derived SiOC aerogels and their application as anodes for Na-ion batteries

Marco Melzi d'Eril [a,*], Andrea Zambotti [a,b,**], Magdalena Graczyk-Zajac [a,d], Emanuel Ionescu [a,c], Gian Domenico Sorarù [b,e], Ralf Riedel [a]

[a] *Institute of Materials Science, Darmstadt University of Technology, Otto-Berndt-Str. 3, 64287, Darmstadt, Germany*
[b] *Department of Industrial Engineering, Glass & Ceramics Laboratory, University of Trento, Via Sommarive 9, 38123, Trento, Italy*
[c] *Fraunhofer Research Institution for Materials Recycling and Resource Strategy, Brentanostr. 2a, D-63755, Alzenau, Germany*
[d] *EnBW Energie Baden-Württemberg AG Durlacher Allee 93, 76131, Karlsruhe, Germany*
[e] *Natl Res Council Italy ICMATE CNR, Inst Condensed Matter Chem & Technol Energy, Via Marini 6, I-16149, Genoa, Italy*

ARTICLE INFO

ABSTRACT

In the last decade, Sodium-Ion-Batteries (SIB) started to gain interest as a possible complementary candidate to support the overburdened lithium technology, but the manufacturing of a proper anode material is one of the challenging factors for the development of performing SIB. Among others, porous polymer-derived ceramics have been widely explored as suitable anodes despite the production of such materials being time and energy-consuming. In this work, we investigate the feasibility of adopting a low-cost ultra-fast high-temperature pyrolysis for the ceramic conversion of a polymer-derived SiOC aerogel to be employed as anode material. A comprehensive study including N_2 physisorption, ^{29}Si MAS NMR and Raman spectroscopy provides the insights of the effect of ultra-fast and conventional heating rates (i.e., 200 $°C·s^{-1}$ vs. 5 $°C·min^{-1}$) on the microstructural features and ceramic yield of the SiOC aerogels. As a consequence of the ultra-fast heating rate, a compositional drift towards oxygen-rich SiOC is observed and discussed. The electrochemical performance of both ceramics has been tested and related to the observed compositional differences, revealing a stable capacity of 103 $mAh·g^{-1}$ for the ultra-fast pyrolyzed SiOC anode, and 152 $mAh·g^{-1}$ for SiOC ceramized at 5 $°C·min^{-1}$.

1. Introduction

With the breakthrough of the electronic age, portable energy sources began to play a fundamental role in society's everyday life, challenging the research to keep pace with the ever-growing need for higher capacities. The possibility of a long-term storability of clean energy as well as the large-scale deployment of electric vehicles would be undoubtedly greatly beneficial for the environment [1,2]. The downside might be a severe overload in the demand for raw materials (i.e. Li and Co) supplies [3], thus strongly soliciting the research to seek for alternatives based on non-critical materials. Sodium-ion batteries (SIBs) are among the potential solutions given the similarities between Na and Li ions and might serve as a viable highly abundant and low-cost alternative to the overburdened reservoirs of raw materials that lithium-ion batteries (LIBs) depend on [4]. Sodium is a highly abundant and cheap element and allows the coupling of aluminium as a current collector for both poles of

the battery, thus further narrowing the costs [5]. Nevertheless, Na does not form a stable compound with graphite [6], making the most widely used anode material for LIBs unsuitable for such purposes hence the difficulty in finding a substitute for the anodic side. In the last decade, various anodic materials ranging from hard carbon [7] to alloying elements including antimony, tin [8] and phosphorus [9] have been broadly investigated. An additional solution is represented by Si-based polymer-derived ceramics (PDCs), which have already proven their applicability both for Li and Na batteries [10,11]. Although several studies demonstrated the high irreversibility of the first insertion [12], the inertness toward other components in the battery, the light weight and the stable cyclability made this class of materials an attractive substitute for graphite for sodium-ion batteries (SIBs).

The chemistry behind polymer-derived ceramics is a matter of study since the early 1970s, making it possible to synthesize complex ceramic systems such as SiCN, SiBCN, and SiAlON, all possessing unique

---

combinations of thermal and chemical inertness, reduced viscous creep at high temperatures and, depending on the elements present in the ceramic system, functional properties that make these materials intriguing for the energy and environmental sectors [13–15]. Among them, polymer-derived ceramic aerogels became a subject of interest as they represent a low-density and high surface area solution for catalysis reactions, thermal insulation, gas separation, water purification and, as recently proven, anodes for LIBs [16,17]. In this framework, the present work deals with the use of a highly porous polymer-derived SiOC aerogel as an anode for sodium-ion batteries. The SiOC aerogels have been obtained using conventional pyrolysis and an ultra-fast pyrolysis (UFP) with a heating rate of 5 °C/min and 200 °C s^{-1}, respectively. Both ceramic aerogels have been carefully characterized to investigate whether the UFP [18] may modify the composition/structure/microstructure and to compare their electrochemical performance as anodes for SIBs. To the best of our knowledge, this is the first study investigating the role of UFP on the ceramization of Si-based polymers.

2. Materials and methods

2.1. Synthesis of the silicon oxycarbide aerogels

Preceramic aerogels were synthesized using Polyramic™ SPR-036 polysiloxane (Starfire Systems Inc NY, USA) as a precursor for the SiOC network. In addition, divinylbenzene (DVB, Sigma Aldrich, CAS: 1321-74-0) was added in a 1:1 wt ratio with SPR-036 to serve both as a crosslinking agent and free carbon source. The two reagents were diluted and mixed for 5 min in a 90%*vol* solution of *n*-hexane (Panreac, CAS: 110-54-3), adding platinum Karstedt's catalyst (Sigma-Aldrich, Saint Louis, MO, USA, CAS: 68,478-92-2) to activate hydrosilylation reactions between the two reagents. To avoid inhomogeneities in the final gel, the platinum catalyst was diluted to 0.1% in xylene before adding it with a ratio of 50 µl per gram of SPR-036 to the diluted reagents mix. Gelation was further induced by sealing the mix in a digestion vessel (Model 4749, Parr Instrument Company, Moline, IL, USA) and holding it at 180 °C for 24 h.

A typical post-gelation treatment of the sample was based on a multi-step solvent exchange: firstly, the wet gel was soaked in fresh *n*-hexane to eliminate unreacted species. Subsequently, it was placed in a customized supercritical reactor to completely substitute the organic solvent with liquid carbon dioxide. Finally, supercritical drying was performed at 42 °C, releasing gaseous CO_2 at a rate <1 bar min^{-1} to avoid decompression cracks on the drying aerogel [19]. This procedure is described more in detail elsewhere [20,21].

Samples of ceramic SiOC aerogels were prepared via pyrolysis in argon at 1000 °C. According to the experimental setup, two different furnaces were used for this purpose. A conventional tubular furnace was employed to heat treat preceramic samples (contained in a quartz

Schlenk tube) at 5 °C·min^{-1} (equivalent to 0.083 °C s^{-1}) up to 1000 °C, with a dwell time of 1 h at the maximum temperature. On the other hand, a customized ultra-fast furnace (Fig. 1) was adopted to pyrolyze preceramic samples at up to 1000 °C, with heating rates of around 200 °C s^{-1} and a dwell time of 40s. It is worth noticing that the heating rate of the UFP is approximately 2500 times higher than that of the conventional pyrolysis process.

The temperature profile of the ultra-fast furnace was acquired at T > 700 °C with a pyrometer (KRTD 1485, Maurer, Germany) positioned outside a glass window of the furnace and calibrated with an effective emissivity of 0.69. The emissivity was calculated considering that of the utilized graphite (heating element) and considering also the transmittance of the glass window. Preceramic samples with a maximum thickness of 2 mm were positioned inside a graphite sandwich (made out of two foils), in correspondence with the pyrometer's measuring spot. Each utilized graphite foil had a rectangular geometry of 1.5 × 9 cm^2, with a thickness of 0.25 mm (Sigratherm®, SGL Carbon, Wiesbaden, DE).

2.2. Structural characterization of the aerogels

Nitrogen physisorption measurements were performed with an Autosorb iQ analyser (Anton-Paar, Gratz, AU) in the $10^{-6} \leq P/P^0 \leq 1$ range. A Non Local Density Functional Theory (NLDFT) approach was utilized for the pore size distribution in the mesopore-micropore range, imposing silica with cylindrical pores as an adsorption model. Calculations were limited to the adsorption branch of each acquired isotherm.

The skeletal densities of the ceramic aerogels were determined via pycnometer using an AccuPyc 1330 pycnometer (Micromeritics, Norcross, GA, USA) at 1.58 bar and 23 °C.

Scanning Electron Microscopy (SEM) micrographs were obtained with a JEOL JSM 7600 F equipped with a Schottky emitter after sputtering with Pt to prevent charging during the observation.

Infrared spectra were acquired in attenuated total reflectance (ATR) mode with a Varian 670-IR spectrometer in the 550-4000 cm^{-1} wavenumber range. A resolution of 4 cm^{-1} and a total of 64 scans per spectrum were imposed.

Raman spectra were collected with a LabRAM Horiba HR spectroscope HR800 (Horiba Jobin Yvon GmbH) spectrophotometer equipped with a green 514.5 nm laser source (Cobolt Fandango™ 100). A total of 3 spectra per sample were acquired in the 0-4000 cm^{-1} range.

Solid-state ^{29}Si Nuclear Magnetic Resonance (NMR) was employed to define the local environment around the silicon atoms. The analyses were carried out with a Bruker 400 W B instrument operating at a proton frequency of 400.13 MHz. The NMR spectra were acquired by adopting a^{29}Si frequency of 79.48 MHz, a $\pi/4$ pulse length of 2.2 µs, and an imposed recycle delay of 200s. A total of 2 k scans per sample were acquired. 4 mm zirconia rotors were used at a 7 kHz spinning frequency
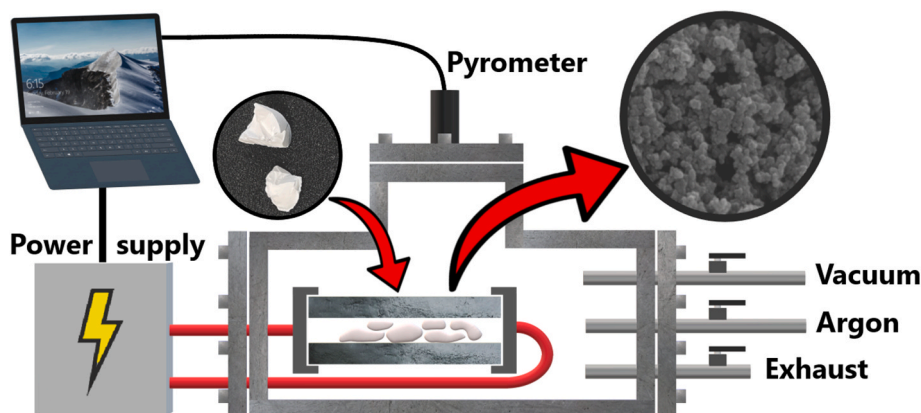

Fig. 1. Scheme of the UFP system used for this work.

under air flow for the analysis. Q8M8 was used as an external secondary reference.

Chemical analyses were carried out on commission by the Micro-analytisches Labor Pascher laboratory via ICP measurements.

2.3. Electrochemical characterization of the aerogels

Electrochemical testing required the preparation of an electrode slurry. The first step consisted of grinding the PDC in a mortar and subsequently with a ball mill (Rocker Mill MM 400, Retsch GmbH, Germany) for 1 h at a frequency of 30 Hz using zirconia milling balls and sieving it down to 40 μm. Carbon black (TIMCAL Super P Conductive Carbon Black) was added to increase the conductivity. The powder was eventually dispersed in a mixture of water-based binders consisting in a 5 wt.% solution of carboxymethylcellulose (CMC, Sigma–Aldrich, UK) in water with the addition of a 40 wt.% solution of styrene-butadiene rubber (SBR, ZEON, Japan) in water/ethanol to increase the adhesion and mechanical stability of the printed slurry. A ratio equivalent to 94/2/2/2 wt.% of respectively active material/carbon black/CMC/SBR was chosen to maximize the energy density of the electrodes. The slurry was printed on an aluminium foil (99,8%, Alfa Aesar) setting a thickness of 120 μm with a doctor blade. After drying the foil with the slurry at 40 °C for some hours the electrodes were cut using a 10 mm diameter cutter. The round electrodes were further dried in a vacuum oven (Büchi B-580 Glass Oven) at 80 °C for 24 h to completely remove the water and were ultimately stored in a glove box under Ar atmosphere. The electrochemical tests have been carried out using Swagelok-type cells as a holder in a two electrodes half-cell configuration. A slice of metallic Na (99,8%, Alfa Aesar) cut to fit in the cell was utilized as a counter-electrode and as a reference. From this point, all the mentioned voltages are to be referred to as vs. Na/Na+. A separator made out of glass fiber (Whatman GE Healthcare) was placed between the metallic sodium and the working electrode and was wetted with 180 μl of a 1 M solution of $NaPF_6$ in EC/DEC 3:7 + 5 wt.% FEC. The electrochemical measurements were carried out using a WMP3 potentiostat (BioLogic GmbH, France) with the cells cycling in an incubator at the stable temperature of 25 °C. Each PDC was tested with galvanostatic cycling with potential limitation (GCPL) performed under a constant current value of 37.2 mAg^{-1} in a voltage range constrained between 2.5 V and 0.005 V for 100 cycles.

3. Results and discussion

3.1. Effect of the heating rate during ceramization on the composition and structure of the as-prepared aerogels

During the ceramization process, silicon-based polymer-derived ceramics undergo weight loss due to the evolution of Si-containing molecular compounds formed by redistribution reactions and $H_2/CH_4/$ small hydrocarbons produced by radical reactions [22,23]. In general redistribution reactions occur in a lower temperature range (ca. 400–600 °C) while radical reactions, having a higher activation energy, start to be active at higher temperatures (ca 600–900 °C). A clear example of the volatile compounds observed during pyrolysis is given by the evolution of silanes, methylsilanes, ethane, methane and hydrogen during the formation of the ceramic network from a methyl-silsesquioxane precursor [24,25].

While numerous studies on the ceramization of polysiloxanes have been published, little attention has been given to the possible effects of the pyrolysis heating rate on the composition and microstructure of the resulting SiOC [26–29]. Therefore, it is worth considering whether the heating rate of the pyrolysis influences the ceramic yield and the microstructure of the final ceramic component. As a matter of fact, one can expect that ultra-fast pyrolysis, owing to the huge amount of energy that is provided to the sample per unit of time, may hinder, boost or even activate certain types of ceramization reactions which, in turn, may affect the composition and microstructure of the resulting ceramic.

Structural parameters which are anticipated to heavily depend on the pyrolysis heating rate may be the porosity and the specific surface area of the resulting ceramic aerogels. Nitrogen physisorption was adopted as an analysis method to investigate the evolution of specific surface area (SSA), pore size and pore volume of the aerogels under different heating rates. The adsorption-desorption isotherms and the NLDFT pore size distributions are reported in Fig. 2. Numerical data are tabulated in Table 1. The two isotherms are comparable in terms of shape and can be assigned to hybrid Type II-Type IV isotherms with a slim reversible hysteresis loop given by capillary condensation in mesopores [30]. As given in Fig. 2c, the pore size distribution of both samples covers the whole range of mesoporosity and continues in the macroporous range, while no microporosity can be observed. The SSAs of the two ceramic aerogels are comparable, with values of 206 $m^2 g^{-1}$ and 196 $m^2 g^{-1}$ for the conventionally and ultra-fast pyrolyzed samples, respectively. On the other hand, the pore size distribution seems to be affected by the heating rate. Fig. 2c reveals that the total porosity curves of the two samples are identical up to ca. 25 nm then, for pores of larger size, the UFP samples show lower porosity compared to the one obtained at 5 °C·min^{-1}. Albeit it is not easy to rationalize this result, mainly because the pore size during pyrolysis can decrease due to a combination of shrinkage and sintering, still we can say that similar results (lower porosity in SiOC pyrolyzed at higher heating rates - i.e., 2 K·min^{-1} - compared to same samples treated at lower HR – i.e., 0.1·min^{-1}) have been already reported in the literature [29].

The skeletal densities of the two ceramic aerogels eventually resulted comparable (see Table 1) suggesting similar free volumes of the silicon oxycarbide glasses, the Schlenk tube sample pyrolyzed at 5 °C·min^{-1} being slightly denser than the UFP one. Both skeletal densities fall in the typical range of similar PDC SiOC aerogels [20,21].

The microstructural features of the aerogel after conventional and ultra-fast ceramization can be observed from Fig. 3a and b respectively. As suggested by N_2 physisorption calculations, the ultra-fast treatment seems to deprive the aerogel of a certain fraction of macropores, which can still be observed but are less visible with respect to the sample treated at 5 °C·min^{-1} (Fig. 3b). From these micrographs, it is evident that the aerogels contain large macropores that exceed 100 nm of diameter that were not detected by the N_2 physisorption measurements. Nevertheless, ultra-fast pyrolysis does not affect the colloidal structure of the polymer-derived aerogel, apparently preserving the dimensions and the shape of the colloidal particles.

Infrared spectra (Fig. 4) acquired on the ceramic samples show no traces of preceramic species, such as organic and silyl groups, confirming that the ultra-fast heat treatment can induce a complete ceramization within 40 s at 1000 °C. Both spectra are characterized by the presence of broad absorption peaks of *Si*–O bending (815 cm^{-1}), O–Si–O asymmetric stretching (1025 cm^{-1}) and C]C stretching at 1537 cm^{-1}, respectively [31,32]. Although no *Si*–C bonds are clearly arising from these infrared spectra, it is known that, in SiOC, the wide absorption region between 1100 and 800 cm^{-1} finds some absorbance contributions from *Si*–C bond deformation at around 880 cm^{-1}, which leads to the pronounced superimposition of the two absorptions signals assigned to *Si*–O bonds [33,34].

The presence of a segregated carbon phase was confirmed by Raman acquisitions on both SiOC samples. In Fig. 5, it is evident the presence of disordered sp2-hybridized turbostratic carbon generated after pyrolyzing SPR-036 crosslinked with DVB at 1000 °C. Raman spectra are characterized by D and G bands at 1340 cm^{-1} and 1590 cm^{-1}, respectively, which are accompanied by smaller peaks assigned to amorphous carbon (a-C) (1140 cm^{-1} and 1510 cm^{-1}). The presence of amorphous carbon has been already reported for SiOC films derived from similar resins, and its peak at 1140 cm^{-1} has been attributed to the presence of sp^3 domains [35]. The deconvolution of all Raman signals was performed using a combination of 8 Gaussian and Lorentzian peaks with Raman shifts and full widths at half maxima (FWHM) according to the
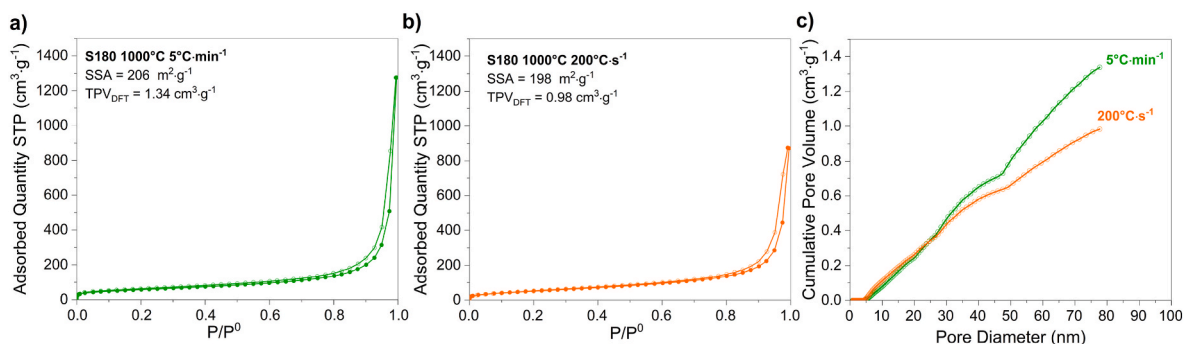
Fig. 2. N$_2$ physisorption isotherms and pore size distributions of the two ceramic aerogels: a) conventionally pyrolyzed at 5 °C·min^{-1}; b) ultra-fast pyrolyzed at 200 °C·s^{-1}; c) comparison of the two DFT cumulative pore size distributions.

Table 1
Resulting SSA, DFT pore volume and skeletal density of the two ceramic aerogels.

Heating rate	SSA (m^2·g^{-1})	Pore Vol. (cm^3·g^{-1})	ρ_s (g·cm^{-3})
5 °C·min^{-1}	206	1.34	1.89
200 °C·s^{-1}	198	0.98	1.79

work of Larouche et al. [36]. In particular, the first 4 peaks were employed to deconvolute the D and G bands, while the other 4 were used in the second-order signals between 2250 and 3250 cm^{-1}, where the T + D, 2D, D + G and 2G overtones appear [37]. The details of the deconvolutions are given in Table 2.

The deconvoluted areas were used as calculation parameters for the definition of L_a and L_{eq}, namely the lateral crystal size and the average continuous graphene length of a domain characterized by tortuosity, as proposed by Larouche et al. [36]. The lateral crystal size L_a was calculated using the Cançado correlation, which suitably adapts to free carbon-containing SiOC glasses [38,39]. The two relations are given in Equation 1, and 2, where λ is the laser wavelength, and the factor 2 in Equation (2) is relative to the two phonons generated by each phonon in the second order signals. It must be said that for these calculations the integrated areas of deconvoluted peaks were used to take into account the uncertainties of the measurements and that each of the values reported in Table 3 was defined after averaging the resulting areas of 3 different acquisitions per sample, to account for any inhomogeneity in the materials. The results displayed in Table 3 show slightly smaller L_a and L_{eq} in the case of ultra-fast pyrolysis, suggesting a higher level of defectiveness in the crystallized nanodomains.

$$L_a = \left(2.4 \cdot 10^{-10}\right)\lambda^4 \left(\frac{A_D}{A_G}\right)^{-1} nm \tag{1a}$$

$$L_{eq} = 2 \cdot \left(2.4 \cdot 10^{-10}\right)\lambda^4 \left(\frac{A_{2D}}{A_D}\right) = 33.6343 \left(\frac{A_{2D}}{A_D}\right) nm \tag{2a}$$

The solid-state ^{29}Si MAS NMR spectra of the preceramic and ceramic samples are shown in Fig. 6a and b The Si coordination of the preceramic network follows that of the SPR-036 precursor, showing a strong resonance at −20.4 ppm that can be associated with D (SiC$_2$O$_2$) units [40]. A secondary resonance peak at −36.7 ppm is relative to D^H (SiHCO$_2$) units. The fact that D^H units are visible means that the hydrosilylation reaction with vinyl units is not fully completed after gelation (confirmed by the ^{13}C CPMAS acquisition given in Figure S1 in the *Supplementary Information*, which clearly shows resonance peaks of residual vinyl groups).
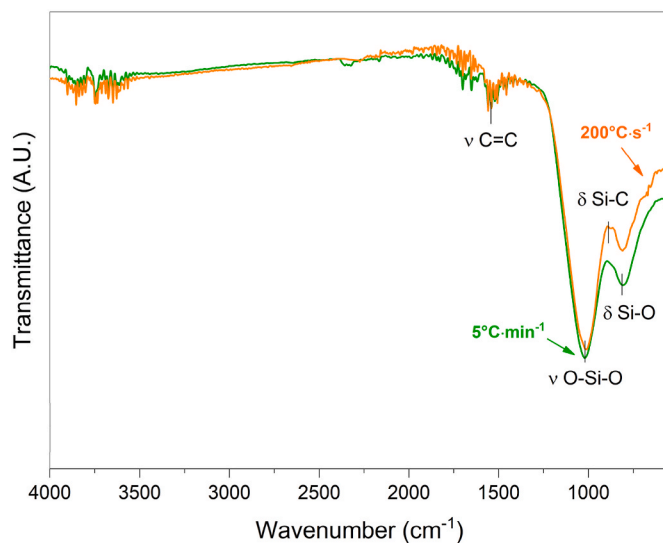

Fig. 4. ATR infrared spectra of the synthesized ceramic samples. The green curve corresponds to the conventionally pyrolyzed sample; whereas the orange curve corresponds to the UFP-treated aerogel. (For interpretation of the references to colour in this figure legend, the reader is referred to the Web version of this article.)
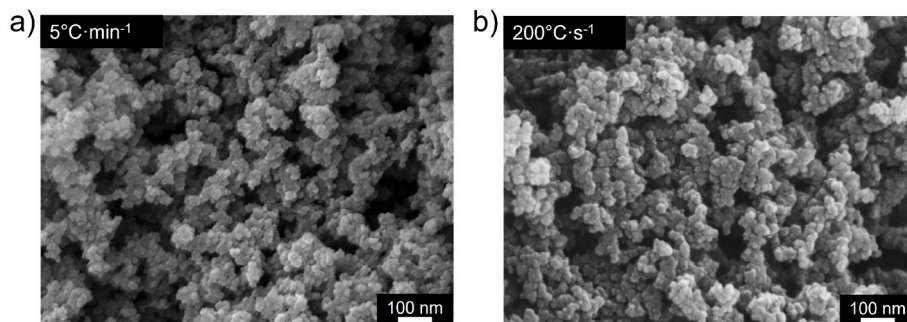

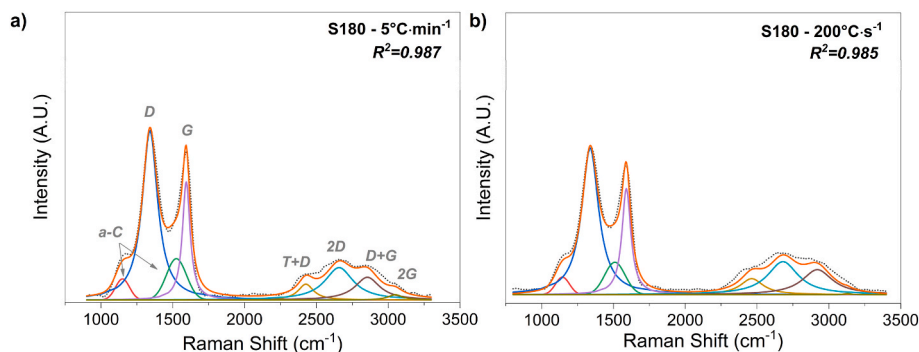**Fig. 3.** FE-SEM micrographs of the ceramic aerogels: a) Heat treated at 5 °C·min^{-1}; b) Heat treated at 200 °C·s^{-1}.

Fig. 5. Deconvoluted Raman spectra of the two ceramic aerogels: a) Heat treated at 5 °C·min^{-1}; b) Heat treated at 200 °C·s^{-1}. In both spectra, the dotted line is the baseline-corrected raw spectrum.

Table 2

Specifications of the deconvolution parameters used in this work. The ranges of Raman shift and FWHM are taken directly from the outcome of deconvolution performed according to the literature [13].

Deconvolution peak	Band shape	Raman shift (cm^{-1})	FWHM (cm^{-1})
a-C	Gaussian	1135–1150	115
D	Lorentzian	1336–1341	130–148
a-C	Gaussian	1510–1525	165
G	Lorentzian	1590–1594	65–70
T + D	Lorentzian	2427–2469	131–213
2D	Lorentzian	2658–2680	239–280
D + G	Lorentzian	2855–2915	209–270
2G	Lorentzian	3050–3240	123–200

Table 3

Main calculated parameters of nanocarbon domains from Raman acquisitions.

Heating rate	A(G)/A(D)	A (2D)/A(D)	L_a (nm)	L_{eq} (nm)
5 °C·min^{-1}	0.38 ± 0.02	0.52 ± 0.21	6.41 ± 0.02	17.4 ± 0.2
200 °C·s^{-1}	0.32 ± 0.03	0.39 ± 0.06	5.34 ± 0.03	13.1 ± 0.1

Fig. 6a unveils other two weak resonance peaks centred at −7.5 and −64.9 ppm, relative to the presence of M (SiOC$_3$) and T (SiCO$_3$) units, which can be attributed to terminal silicon atoms and *Si*–H moieties oxidized into *Si*–O ones.

At least three resonance peaks can be attributed to each ceramic aerogel. According to the chemical shift of −35, −70 and −110 ppm, these resonance signals can be attributed to D, T and Q (SiO$_4$) units, respectively [41]. The spectra show a poor signal-to-noise ratio typical for these materials however it is still possible to appreciate a shoulder of the Q peak at −125 ppm, especially in the sample pyrolyzed at 5 °C·min^{-1}, which has been attributed to silica tetrahedra with distorted

bonds (i.e., with an angle distribution centred at 158.4°), and that has been already observed in high free carbon-containing SiOC and porous zeolites provided with channels, voids and cages [42].

Table 4 summarizes the fractions of *D, T* and *Q* units found in the two SiOC aerogels. The fraction of *T* units is slightly more pronounced in the ultra-fast pyrolyzed sample. The starting precursor is predominantly a linear polymer formed by silicon units bonded to two oxygen atoms with H, CH$_3$ and CHCH$_2$ lateral groups. According to conventional silicone nomenclature, functional units are designated by capital letters, indicating oxygen functionality, i.e. the number of bridging oxygens, and by a superscript referring to the type and number of functional groups bonded to the silicon atom (e.g. *Si*-X where X: H, OH, etc.); the methyl groups are omitted. Acronyms used are: Q, SiO$_{4/2}$; T^H, HSiO$_{3/2}$; T, CH$_3$SiO$_{3/2}$; D^H, H(CH$_3$) SiO$_{2/2}$; and D, (CH$_3$)$_2$SiO$_{2/2}$. Accordingly, in the starting precursor mainly D^H and D units should be present. The redistribution reactions, also called "scrambling reactions", are active in the temperature range 400–700 °C and allow the formation of T and Q units (note that when starting from D^H unit, M^H or T^H units should form, as reported in **Reaction 1, 2**) [43]:

$$2D \rightarrow M + T \tag{1b}$$

$$2T \rightarrow D + Q \tag{2b}$$

Interestingly, the experimental result shows a substantial

Table 4

Chemical shift (δ), atomic fraction and peak assignment of the^{29}Si MAS spectra.

δ (ppm)	S180 - 200 °C·s^{-1}	S180 - 5 °C·min^{-1}	
	Units fraction (%)		
−35	20	27	*D* (SiC$_2$O$_2$)
−70	32	19	*T* (SiCO$_3$)
−110	48	54	*Q* (SiO$_4$)

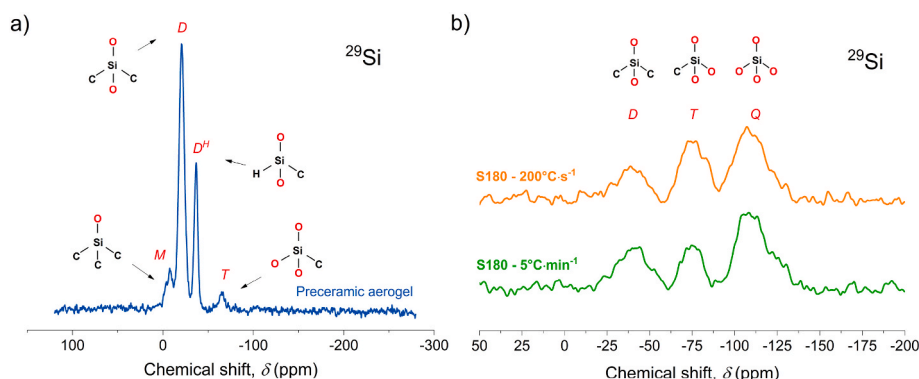**Fig. 6.** ^{29}Si MAS NMR spectra of a) preceramic aerogel; b) ceramic aerogels featuring D, T and Q units.

quantitative equivalence of the different Si sites as a function of the heating rate, with a slight predominance of T units in the UFP sample, suggesting that these reactions are not kinetically controlled and the driving force must be attributed to the corresponding increase in entropy [22]. The ceramic yield of ultra-fast and conventionally pyrolyzed aerogels results of 56% and 65.4%, respectively, suggesting that different oligomers might have escaped the transforming networks as a consequence of the huge difference in the delivered thermal energy densities upon pyrolysis. By comparing Fig. 6a and b, it is clear that the formation of Q units from the D + D^H configuration of the preceramic aerogel can occur within 40 s of ultrafast pyrolysis. The absence of a clear difference between the spectra of the two samples confirms that the surroundings of silicon atoms, which are determined by entropically controlled redistribution reactions of *Si*–O, *Si*–C and *Si*–H [43], are able to evolve as fast as the imposed ultra-fast heating. These redistribution reactions are known to reach a metastable equilibrium below 1000 °C.

The values listed in Table 5 allow a comparison of the elemental composition of the samples S180 - 200 °C·s^{-1} and S180 - 5 °C·min^{-1}. The percentage of Si is almost identical in both samples, whereas the values of oxygen and carbon slightly differ. The SiOC sample obtained at 5 °C·min^{-1} contains circa 10% more free carbon and 2.4% less oxygen than the ultra-fast pyrolyzed one. Considering the stoichiometric formula SiC$_x$O$_{2(1-x)}$ [44], the amount of free carbon in the SiOC matrix can be calculated. Accordingly, most of the carbon belongs to its segregated phase, while just a fraction bonds to silicon. Considering the two compositions found in Table 5, the UFP sample has a slightly lower amount of bonded C (0.19 vs. 0.25) compared to the conventionally pyrolyzed one while the amount of free C is very close to each other. Residuals from the chemical analyses account for 2.41 wt.% and 2.01 wt.% in the sample treated at 200 °C·s^{-1} and 5 °C·s^{-1}, respectively. In these quantities we cannot exclude a certain fraction of residual hydrogen, as indirectly suggested by the weak FT-IR signal of residual aromatic C]C in Fig. 4.

Given all of the above, we propose a possible mechanism that could explain the differences found in the two samples. It is known that in similar systems, namely in methyl-silsesquioxanes, redistribution and ceramization reactions fall in a similar range of temperatures. This was confirmed via TG-MS studies conducted by Campostrini et al. on the evolution of reaction products from methyl-silsesquioxanes under ceramization [24]. In particular, methyl silane and hydrogen are formed in the 700–800 °C range, and are the product of a redistribution and a ceramization reaction, respectively. These two reactions are given in Fig. 7. While redistribution reactions are entropically driven, and thus not dependent on the heating rate of the pyrolysis, ceramization reactions involve the formation of new bonds, so that the reacted fraction of bonds, given such a reaction, is a function of time, and thus of heating rate [22,43]. In general, this dependence is exploited in rate-isoconversion methods for the determination of the activation energy of reactions [45]. This means that the reaction generating a carbon bond and molecular hydrogen would be shifted to a higher temperature range compared to the other one. Now, in a conventional pyrolysis at 5 °C·min^{-1}, these two reactions are concurrent, so that any methyl group which already reacted with a silyl group forming a *Si*–CH$_2$–Si bridge will not take part in the redistribution reaction and consequently will not form a methylsilane which could ultimately escape the system. As a result a higher ceramic yield is expected (i.e. 65.4%) compared to the case of an ultra-fast pyrolysis, where the redistribution reaction (Fig. 7a)

can occur already at 700–800 °C, with no concurrent consumption of methyl groups by the subsequently occurring ceramization reaction (Fig. 7b). As an overall effect of ultra-fast conditions, a lower ceramic yield is expected (i.e. 56.0%), and a smaller fraction of bonded carbon is observed, together with a slightly higher oxygen content due to the loss of silicon, too. Besides, an indirect confirmation of this possible mechanism is given by N$_2$ physisorption (Fig. 2c), which reports a smaller pore volume in the UF pyrolyzed aerogels, and ^{29}Si NMR (Fig. 6b), where a notable fraction of SiO$_4$ units results deformed after a conventional pyrolysis. In fact, both of these effects might be directly linked to the viscosity evolution in the SiOC network under formation: in the conventionally pyrolyzed aerogels, the density of bonds increases at lower temperatures thanks to the ceramization reaction starting at 700 °C. This clearly increases the viscosity of the SiOC network at an early stage, eventually leading to a smaller shrinkage (i.e., higher pore volume) and a more distorted network (Fig. 6b, shoulder at −125 ppm of the Q unit in S180 5 °C·min^{-1}).

In conclusion, despite the huge difference in heating rate during pyrolysis, around 4 orders of magnitude from 0.083 up to 200 °C s^{-1}, the experimental results reveal only subtle differences between the two studied samples. The SSA is the same, around 200 m^2 g^{-1}, while the porosity is slightly lower for the UFP samples which display smaller fraction of large pores above 25 nm. The colloidal particle size, as revealed by SEM, is not affected by the heating rate. Raman spectroscopy suggests that the free C phase of the UFP sample has a slightly higher level of defectiveness in the crystallized nanodomains compared to the conventional pyrolyzed one. The ^{29}Si MAS NMR investigation resulted in very similar spectra characterized by the presence of D, T and Q units in similar amounts while the chemical analysis suggested the same amount of free C phase with a slightly higher amount of bonded carbon in the amorphous silicon oxycarbide network. These results point out the possibility to obtain a ceramic with comparable characteristics with a lower effort in terms of time and energy consumption.

3.2. Electrochemical characterization of the prepared aerogels

The first sodiation of the sample S180 - 5 °C·min^{-1} shows a capacity of 867 mAh·g^{-1} of which 183 mAh·g^{-1} could be reversibly desodiated. Also, the sample pyrolyzed in the UFP furnace displays a low reversibility in the first cycle reaching a capacity equal to 738 mAh·g^{-1} during the sodiation whereas a desodiation capacity of 125 mAh·g^{-1} was registered.

The low reversibility of the first sodiation shown by both samples is well known for this type of material and partially results from the formation of the Solid Electrolyte Interface (SEI) which covers a high surface area due to the mesoporous characteristic of the matrix [46,47]. Another mechanism responsible for the capacity loss is the partial reversibility of the electrochemical redox process taking place in the first cycle as explained by Dou et al. [48]. Micropores are also known to be trapping the cations during the first cycle [46] but their absence confirmed by the gas adsorption analysis excludes this mechanism as partly responsible for the high irreversibility registered. Although both samples performed stably for 100 cycles (see Fig. 8), the registered capacity after 100 cycles is significantly higher for the sample pyrolyzed in the Schlenk tube. Additional information on the rate capacity measurements are given in **Figure S2** in the *Supplementary information*.

The ultra-fast and conventionally pyrolyzed samples present C$_{free}$

Table 5
Weight and molar composition of the two analysed samples.

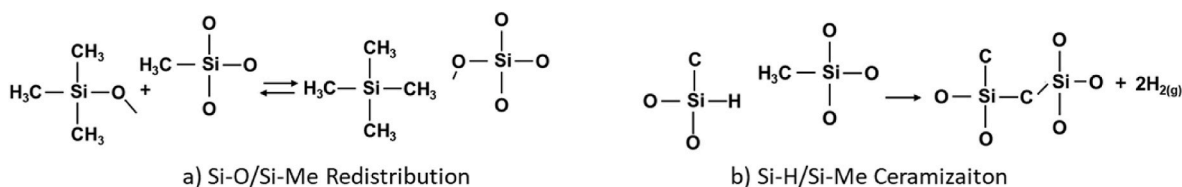| Sample	S180 - 200 °C·s^{-1}			S180 - 5 °C·min^{-1}		
Element	C	O	Si	C	O	Si
Weight %	35.32 ± 0.11	29.92 ± 0.04	32.35 ± 0.07	38.36 ± 0.03	27.53 ± 0.08	32.1 ± 0.28
Moles	2.54	1.62	1	2.78	1.5	1
Derived composition	SiC$_{0.19}$O$_{1.62}$ + 2.35 C$_{free}$			SiC$_{0.25}$O$_{1.5}$ + 2.53 C$_{free}$		

Fig. 7. Concurrent reactions in the SiOC(H) system under evolution in the 700–800 °C range: a) Redistribution of *Si*–O and Si–Me groups; b) Bridging carbon construction via reaction involving *Si*–H and Si–Me bonds.

amounts of 32.4% and 34.6%, respectively. Although the correlation between the free carbon content and the capacity has been reported for similar materials [50,51], the slight difference in the amount of free carbon can only partially justify the higher capacity of the S180 - 5 °C·min^{-1} sample (Table 6).

A typical discharge curve of disordered hard carbons (the free carbon phase in SiOC also belongs to this category) versus sodium metal is composed of a slope region and a plateau region. Those two regions represent an illustration of possible mechanisms, namely the adsorption–intercalation–pore-filling mechanism. In the early model proposed by Dahn and Stevens [52,53], the slope region was attributed to the intercalation of sodium ions into the parallel graphitic layers, and the plateau was assigned to the filling of free space (often called "nanoporosity".

The charge/discharge transients of S180 - 200 °C·s^{-1} and S180 - 5 °C·min^{-1} (compare Fig. 7a and b respectively) present a very similar shape and are mainly composed of the slope region with a very small contribution of the plateau region. Moreover, the charge inserted under 0.5 V, plateau and low voltage region, diminishes from the 2nd to 100th cycle of around 40–50 mA h·g^{-1} indicating that the storage is less reversible. This dominative contribution of the adsorption mechanism signifies that the active surface area of the material will determine the electrochemical storage capacity. Thus, the stable storage capacity is solely settled by the surface properties. Those are mostly determined by the free carbon phase, namely, a thin film of turbostratic carbon is present on the surface of the matrix particles [54]. Sample S180 - 5 °C·min^{-1} contains ca. 10% more of free carbon (compare Table 5).

Table 6
Stoichiometry, free carbon content and Na storage capacity of the known SiOC found in the literature. Free-carbon fraction is calculated according to the elemental composition found in the references.

Sample	Year	Capacity Reported (mAhg^{-1})	C$_{free}$-content (wt.%)	Stoichiometry
SiCO_Ph_T [49]	2015	150 (after 40 cycles) @ 50 mA g^{-1}	37	SiC$_{0.3}$O$_{1.4}$ + 2.89C$_{free}$
SiOC_HC$_G$ [11]	2016	141 (after 50 cycles) @ 37 mA g^{-1}	83.6	SiC$_{0.37}$O$_{0,69}$+ 22.48C$_{free}$
900C-1h-10M [50]	2018	160 (after 200 cycles) @ 25 mA g^{-1}	31.3	SiC$_{1.93}$ O$_{2.07}$ + 3.22C$_{free}$
S180–5°C·min^{-1}	2022	152 (after 100 cycles) @ 37 mA g^{-1}	34.6	SiC$_{0.25}$O$_{1.5}$ + 2.53 C$_{free}$
S180–200°C·s^{-1}	2022	103 (after 100 cycles) @ 37 mA g^{-1}	32.4	SiC$_{0.19}$O$_{1.62}$ + 2.35 C$_{free}$

Raman Spectroscopy results show that the crystallite size L_a is comparable for both materials, however the tortuosity, a continuous domain composed of several crystallites, containing curved graphene sites in-between is higher for S180 - 5 °C·min^{-1} material (17.4 nm in comparison to 13.1 nm for S180 – 200 °C·s^{-1}). We believe, that all those
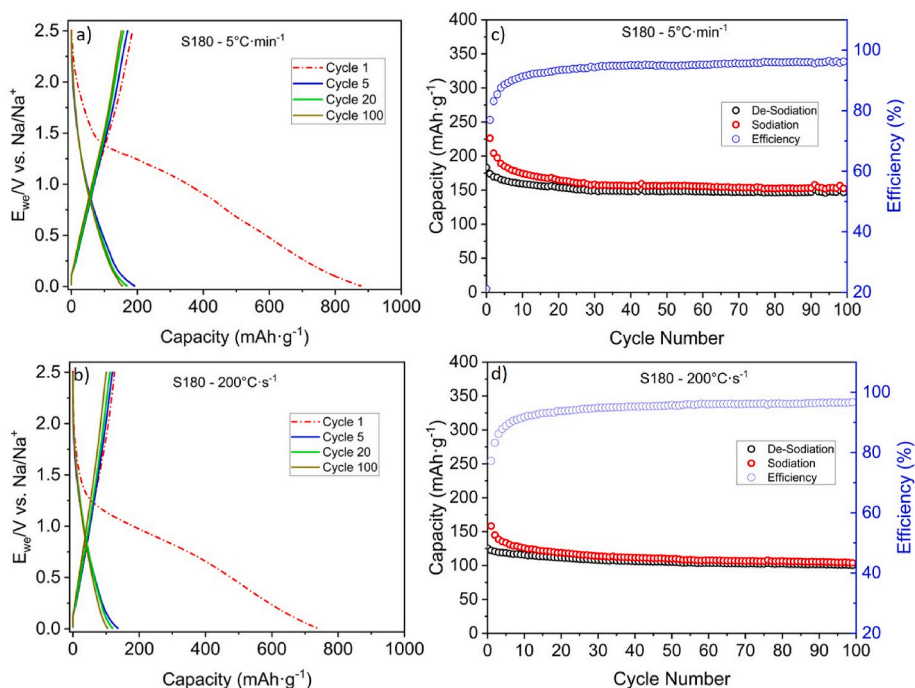

Fig. 8. Voltage vs. capacity curve showing the 1st, 5th, 20th and 100th cycle of the sample S180 - 5 °C·min^{-1} a) and S180 - 200 °C s^{-1} b). Fig. 6c) and d) show respectively the capacity evolution over the time during 100 cycles of S180 - 5 °C·min^{-1} and S180 - 200 °C·s^{-1}..

three factors, namely a higher BET SSA, higher amount of free carbon and higher tortuosity of a free carbon phase lead to the better electrochemical performance of S180 - 5 °C·min^{-1} material.

4. Conclusions

In this work, an aerogel-derived SiOC is pyrolyzed at 1000 °C using two different heating rates, namely 200 °C s^{-1} and 5 °C·min^{-1} (0.083 °C s^{-1}). Despite the four orders of magnitude that differentiate the two heating rates, the two SiOC aerogels resulted comparable in all of the studied microstructural and chemical features, being the ceramic yield of 56% and 65.4%, respectively, the main disparity. According to the ^{29}Si MAS NMR results, it seems that redistribution reactions occur rather easily even under extremely high heating rates, and, overall, the complete polymer-to-ceramic transition can be still achieved within 40s with no significant differences apart from the higher defectiveness of the free carbon phase, which resulted as a minor detrimental effect of UFP, and the slight difference in the carbon content of the two aerogels.

The electrochemical performance of these aerogels as anodes for Na ion batteries was measured and the capacity resulting from the different thermal treatment was discussed. Some concerns regarding the upscalability of the process and the homogeneity of the resulting ceramic remain and could be a topic for future research. However, although the sample pyrolyzed with the UFP furnace shows a lower capacity than for the sample pyrolyzed at 5 °C/min, the stability of the material over 100 cycles makes the ultra-fast pyrolysis a promising approach for cheaper and less time-consuming production of polymer-derived ceramics as anodes for SIBs.

Declaration of competing interest

The authors declare that they have no known competing financial interests or personal relationships that could have appeared to influence the work reported in this paper.

Appendix A. Supplementary data

Supplementary data to this article can be found online at https://doi.org/10.1016/j.oceram.2023.100354.

References

[1] H. Hesse, M. Schimpe, D. Kucevic, et al., Lithium-ion battery storage for the grid—a review of stationary battery storage system design tailored for applications in modern power grids, Energies 10 (12) (2017) 2107.

[2] D. Petrovic, D. Pesic, M. Petrovic, et al., Electric cars: are they solution to reduce CO2 emission? Therm. Sci. 24 (5) (2020) 2879–2889.

[3] C. Grosjean, P.H. Miranda, M. Perrin, et al., Assessment of world lithium resources and consequences of their geographic distribution on the expected development of the electric vehicle industry, Renew. Sustain. Energy Rev. 16 (3) (2012) 1735–1744.

[4] E.A. Olivetti, G. Ceder, G.G. Gaustad, et al., Lithium-ion battery supply chain considerations: analysis of potential bottlenecks in critical metals, Joule 1 (2) (2017) 229–243.

[5] C. Vaalma, D. Buchholz, M. Weil, et al., A cost and resource analysis of sodium-ion batteries, Nat. Rev. Mater. 3 (4) (2018).

[6] H. Moriwake, A. Kuwabara, C.A.J. Fisher, et al., Why is sodium-intercalated graphite unstable? RSC Adv. 7 (58) (2017) 36550–36554.

[7] X. Dou, I. Hasa, D. Saurel, et al., Hard carbons for sodium-ion batteries: structure, analysis, sustainability, and electrochemistry, Mater. Today 23 (2019) 87–104.

[8] W.T. Jing, C.C. Yang, Q. Jiang, Recent progress on metallic Sn- and Sb-based anodes for sodium-ion batteries, J. Mater. Chem. 8 (6) (2020) 2913–2933.

[9] X. Xu, D. Zhou, X. Qin, et al., A room-temperature sodium-sulfur battery with high capacity and stable cycling performance, Nat. Commun. 9 (1) (2018) 3870.

[10] M. Graczyk-Zajac, L. Toma, C. Fasel, et al., Carbon-rich SiOC anodes for lithium-ion batteries: Part I. Influence of material UV-pre-treatment on high power properties, Solid State Ionics 225 (2012) 522–526.

[11] J. Kaspar, M. Storch, C. Schitco, et al., SiOC(N)/Hard carbon composite anodes for Na-ion batteries: influence of morphology on the electrochemical properties, J. Electrochem. Soc. 163 (2) (2016) A156–A162.

[12] M. Graczyk-Zajac, L.M. Reinold, J. Kaspar, et al., New insights into understanding irreversible and reversible lithium storage within SiOC and SiCN ceramics, Nanomaterials 5 (1) (2015) 233–245.

[13] E. Ionescu, S. Bernard, R. Lucas, et al., Polymer-derived ultra-high temperature ceramics (UHTCs) and related materials, Adv. Eng. Mater. 21 (8) (2019), 1900269.

[14] Y. Iwase, Y. Horie, S. Honda, et al., Microporosity and CO2 capture properties of amorphous silicon oxynitride derived from novel polyalkoxysilsesquiazanes, Materials 11 (3) (2018).

[15] P. Colombo, G. Mera, R. Riedel, et al., Polymer-Derived Ceramics: 40 Years of Research and Innovation in Advanced Ceramics, Journal of the American Ceramic Society, 2010 no-no.

[16] C. Vakifahmetoglu, T. Semerci, A. Gurlo, et al., Polymer derived ceramic aerogels, Curr. Opin. Solid State Mater. Sci. 25 (4) (2021), 100936.

[17] V.S. Pradeep, D.G. Ayana, M. Graczyk-Zajac, et al., High rate capability of SiOC ceramic aerogels with tailored porosity as anode materials for Li-ion batteries, Electrochim. Acta 157 (2015) 41–45.

[18] C. Wang, W. Ping, Q. Bai, et al., A general method to synthesize and sinter bulk ceramics in seconds, Science (New York, N.Y.) 368 (6490) (2020) 521–526.

[19] M.A. Aegerter, N. Leventis, M.M. Koebel, Aerogels Handbook, Springer New York, New York, NY, 2011.

[20] A. Zambotti, F. Valentini, E. Lodi, et al., Thermochemical heat storage performances of magnesium sulphate confined in polymer-derived SiOC aerogels, J. Alloys Compd. 895 (2022), 162592.

[21] A. Zambotti, E. Caldesi, M. Pellizzari, et al., Polymer-derived silicon nitride aerogels as shape stabilizers for low and high-temperature thermal energy storage, J. Eur. Ceram. Soc. 41 (11) (2021) 5484–5494.

[22] P.H. Mutin, Role of redistribution reactions in the polymer route to silicon-carbon-oxygen ceramics, J. Am. Ceram. Soc. 85 (5) (2002) 1185–1189.

[23] D. Hourlier, S. Venkatachalam, M.-R. Ammar, et al., Pyrolytic conversion of organopolysiloxanes, J. Anal. Appl. Pyrol. 123 (2017) 296–306.

[24] R. Campostrini, A. Zambotti, M. Biesuz, et al., On the pyrolysis of a methyl-silsesquioxane in reactive CO2 atmosphere: a TG/MS and FT-IR study, J. Am. Ceram. Soc. 105 (4) (2022) 2465–2473.

[25] D. Bahloul-Hourlier, J. Latournerie, P. Dempsey, Reaction pathways during the thermal conversion of polysiloxane precursors into oxycarbide ceramics, J. Eur. Ceram. Soc. 25 (7) (2005) 979–985.

[26] G.D. Sorarù, G. D'Andrea, R. Campostrini, et al., Structural characterization and high-temperature behavior of silicon oxycarbide glasses prepared from sol-gel precursors containing Si-H bonds, J. Am. Ceram. Soc. 78 (2) (1995) 379–387.

[27] G.D. Sorarù, L. Pederiva, J. Latournerie, et al., Pyrolysis kinetics for the conversion of a polymer into an amorphous silicon oxycarbide ceramic, J. Am. Ceram. Soc. 85 (9) (2002) 2181–2187.

[28] S.J. Widgeon, S. Sen, G. Mera, et al., 29 Si and 13 C solid-state NMR spectroscopic study of nanometer-scale structure and mass fractal characteristics of amorphous polymer derived silicon oxycarbide ceramics, Chem. Mater. 22 (23) (2010) 6221–6228.

[29] H. Schmidt, D. Koch, G. Grathwohl, et al., Micro-/Macroporous ceramics from preceramic precursors, J. Am. Ceram. Soc. 84 (10) (2001) 2252–2255.

[30] F. Rouquerol, Adsorption by Powders and Porous Solids: Principles, Methodology and Applications, Elsevier/Academic Press, Amsterrdam, 2014.

[31] D. Assefa, E. Zera, R. Campostrini, et al., Polymer-derived SiOC aerogel with hierarchical porosity through HF etching, Ceram. Int. 42 (10) (2016) 11805–11809.

[32] G.D. Sorarù, K. Girardini, M. Narisawa, et al., Effect of anionic substitution on the high temperature stability of polymer-derived SiOC glasses, J. Am. Ceram. Soc. 104 (7) (2021) 3097–3104.

[33] G.D. Soraru, R. Campostrini, A.A. Ejigu, E. Zera, P. Jana, Preface, J. Ceram. Soc. Jpn. 124 (10) (2016). P10-P11-P10-3.

[34] R. Pena-Alonso, G.D. Soraru, R. Raj, Preparation of ultrathin-walled carbon-based nanoporous structures by etching pseudo-amorphous silicon oxycarbide ceramics, J. Am. Ceram. Soc. 89 (8) (2006) 2473–2480.

[35] P.K. Chu, L. Li, Characterization of amorphous and nanocrystalline carbon films, Mater. Chem. Phys. 96 (2–3) (2006) 253–277.

[36] N. Larouche, B.L. Stansfield, Classifying nanostructured carbons using graphitic indices derived from Raman spectra, Carbon 48 (3) (2010) 620–629.

[37] G. Mera, A. Navrotsky, S. Sen, et al., Polymer-derived SiCN and SiOC ceramics – structure and energetics at the nanoscale, J. Mater. Chem. 1 (12) (2013) 3826.

[38] L.G. Cançado, A. Jorio, E.H.M. Ferreira, et al., Quantifying defects in graphene via Raman spectroscopy at different excitation energies, Nano Lett. 11 (8) (2011) 3190–3196.

[39] E. Ricohermoso III, F. Klug, H. Schlaak, et al., Electrically conductive silicon oxycarbide thin films prepared from preceramic polymers, Int. J. Appl. Ceram. Technol. 19 (1) (2022) 149–164.

[40] P. Dibandjo, S. Diré, F. Babonneau, et al., Influence of the polymer architecture on the high temperature behavior of SiCO glasses: a comparison between linear- and cyclic-derived precursors, J. Non-Cryst. Solids 356 (3) (2010) 132–140.

[41] S. Dirè, E. Borovin, M. Narisawa, et al., Synthesis and characterization of the first transparent silicon oxycarbide aerogel obtained through H 2 decarbonization, J. Mater. Chem. 3 (48) (2015) 24405–24413.

[42] J.P. Nimmo, P. Kroll, First-principles calculations and analysis of 29 Si nuclear magnetic resonance chemical shifts in silicon oxycarbide ceramics, J. Phys. Chem. C 118 (51) (2014) 29952–29961.

[43] R.J.P. Corriu, D. Leclercq, P.H. Mutin, et al., 29Si nuclear magnetic resonance study of the structure of silicon oxycarbide glasses derived from organosilicon precursors, J. Mater. Sci. 30 (9) (1995) 2313–2318.

[44] H. Brequel, G.D. Sorarù, F. Babonneau, et al., Structural properties of silicon oxycarbide powders obtained by SOL-GEL method, J. Metastable Nanocryst. Mater. 2–6 (1999) 411–416.

[45] M. Starink, The determination of activation energy from linear heating rate experiments: a comparison of the accuracy of isoconversion methods, Thermochim. Acta 404 (1–2) (2003) 163–176.

[46] J. Kaspar, M. Storch, C. Schitco, et al., SiOC(N)/Hard carbon composite anodes for Na-ion batteries: influence of morphology on the electrochemical properties, J. Electrochem. Soc. 163 (2) (2016) A156–A162.

[47] F. Béguin, F. Chevallier, C. Vix-Guterl, et al., Correlation of the irreversible lithium capacity with the active surface area of modified carbons, Carbon 43 (10) (2005) 2160–2167.

[48] X. Dou, D. Buchholz, M. Weinberger, et al., Study of the Na storage mechanism in silicon oxycarbide—evidence for reversible silicon redox activity, Small Methods 3 (4) (2019), 1800177.

[49] M. Weinberger, C. Pfeifer, S. Schindler, et al., Submicron-sized silicon oxycarbide spheres as anodes for alkali ion batteries, J. Mater. Chem. 3 (47) (2015) 23707–23715.

[50] C. Chandra, J. Kim, Silicon oxycarbide produced from silicone oil for high-performance anode material in sodium ion batteries, Chem. Eng. J. 338 (2018) 126–136.

[51] J. Kaspar, M. Graczyk-Zajac, S. Choudhury, et al., Impact of the electrical conductivity on the lithium capacity of polymer-derived silicon oxycarbide (SiOC) ceramics, Electrochim. Acta 216 (2016) 196–202.

[52] D.A. Stevens, J.R. Dahn, An in situ small-angle X-ray scattering study of sodium insertion into a nanoporous carbon anode material within an operating electrochemical cell, J. Electrochem. Soc. 147 (12) (2000) 4428.

[53] D.A. Stevens, J.R. Dahn, The mechanisms of lithium and sodium insertion in carbon materials, J. Electrochem. Soc. 148 (8) (2001), A803.

[54] M. Graczyk-Zajac, D. Vrankovic, P. Waleska, et al., The Li-storage capacity of SiOC glasses with and without mixed silicon oxycarbide bonds, J. Mater. Chem. 6 (1) (2018) 93–103.